2026 IEEE International Conference on Robotics and Automation (ICRA 2026)
June 1-5, 2026. Vienna, Austria

Controllable Steering Torque Generation via Flapping Motion by a Cross-Coupled Two-Degree-of-Freedom Drive System*

M. Hamamoto, M. Yamashita, M. Tanaka and K. Senda

Abstract— **We present a novel flapping-wing mechanism capable of generating steering torque through a two-degree-of-freedom (2-DoF) coordinated actuation. Whereas most existing flapping-flight systems produce steering torque by incorporating additional mechanisms that asynchronously alter passive deformation limits, our approach enables transient aerodynamic force modulation synchronized with each flapping stroke. The concept draws inspiration from biological flyers such as dragonflies and hawkmoths, which utilize multiple synchronous muscles per wing and perform stroke-synchronized, multi-DoF wing kinematics—strategies thought to contribute to their precise attitude and position control even at low flapping frequencies. To emulate this capability, we developed a mechanism employing parallel direct-drive actuators within a coupled multi-DoF architecture. By introducing a cross-coupling force between the actuators, we eliminate path dependency in the wing-twist motion, thereby enabling stable and independent control of both stroke angle and angle of attack. Using a single-wing 2-DoF testbed, we successfully demonstrate a lift force exceeding 10 gf and a yaw-steering torque range of 1.5 mNm. This work advances the development of biologically inspired, stroke-synchronized steering mechanisms for next-generation flapping-wing micro aerial vehicles.**

I. Introduction

Drawing inspiration from the remarkable aerial capabilities of birds and insects—including hovering, rapid maneuvering, and reverse flight—researchers have extensively developed artificial flapping mechanisms and constructed flapping micro-aerial vehicles (FMAVs) [1–5]. Recent advancements have enabled robotic systems to realize stable hovering, a complex feat once exclusive to biological flyers. Notably, several studies have demonstrated that such capabilities can be achieved using commercially available electromagnetic actuators [4–7].

Traditionally, flapping motion—characterized by reciprocating movement—has been realized by converting motor rotation through linkage mechanisms [5]. While these systems offer mechanical simplicity and ease of fabrication, they often suffer from motion inaccuracies due to component slack, raising concerns about controllability and long-term durability. Keennon et al. addressed these limitations by replacing conventional linkages with a belt and elliptical pulley system, leading to the development of the first untethered, tailless hovering aircraft [4]. In such systems, the stroke angle typically remains fixed, and attitude control is achieved by adjusting the wing trailing edge support point. In Keennon's FMAV, a primary motor drives the stroke motion, while three tiny servo modules manage attitude control.

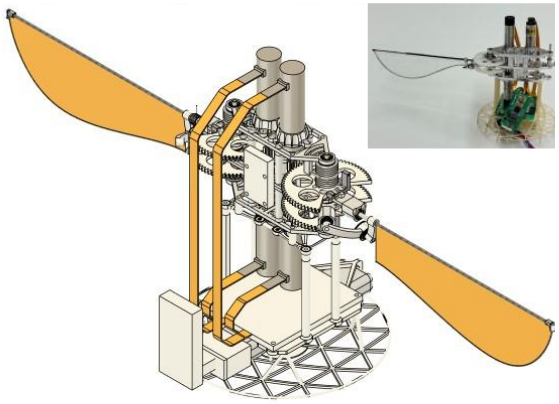

Figure 1. A 2x2-DoF FMAV design. Prototype model is shown in the upper-right inset. (Only the left side components are equipped.)

Insights from biological flight studies suggest that improving mechanical impedance matching between the actuator and wing drive system increases the stroke amplitude, thereby enhancing flight performance [8]. Using piezoelectric bimorph actuators, Wood et al. achieved hovering in a 0.1-g FMAV, albeit with a tethered power supply [9–11]. Building on these findings, Campolo et al. proposed that large stroke amplitudes and high flapping frequencies could be directly achieved via CW/CCW rotation of a DC motor, provided impedance matching is optimized [12, 13]. Zhan et al. subsequently demonstrated untethered hovering using a configuration in which each wing is independently driven by a dedicated motor. This setup enables three degrees of freedom (DoF) in attitude control torque by manipulating stroke amplitude for roll, stroke center offset for pitch, and the speed differential between forward and backward strokes for yaw, respectively [6].

Despite these advances, the degrees of freedom in wing actuation remain limited, significantly constraining flight control capabilities. While simplifying biological flight mechanisms is a core strategy in biomimetic engineering, it often results in the omission of critical flight characteristics necessary for agile maneuvers. Therefore, to realize agile and acrobatic robotic flight, the impact of incorporating additional DoFs warrants thorough investigation. Previously, we tried to build a 2 × 2-DoF FMAV utilizing four ultrasonic motors (USMs) and dual motion conversion mechanisms to enable stroke and flip motions and reported bidirectional driving

*Research supported by Japan Aerospace Exploration Agency (JAXA).

M. Hamamoto, Y. Yamashita, and M. Tanaka are with the R&D Office of Corporate Planning Department, Nakakita Seisakusho Co. Ltd., Daito, Osaka, 574-8691, Japan (phone: +81-72-871-7270, E-mail: m-hamamoto @nakakita-s.co.jp, m-yamashita@nakakita-s.co.jp, m-tanaka@nakakita-s.co.jp)

K. senda is with the Department of Aeronautics and Astronautics, Kyoto University, Kyoto, 615-8540, Japan (E-mail: senda@kuaero.kyoto-u.ac.jp)

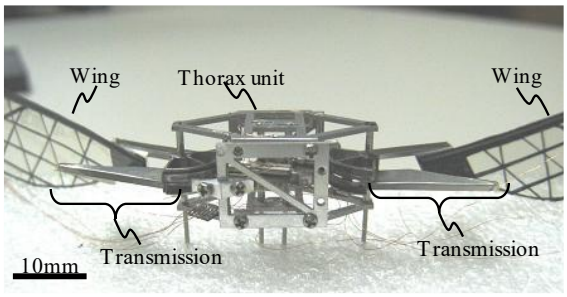

Figure 2. 2x2-DoF USMs-driven prototype [14].

experiment [14]. This effort primarily focused on the application of USMs in FMAVs, without fully addressing the suitability or optimization of the motion conversion mechanism and consequently failed to achieve stable steering.

In this study, we demonstrate that coordinated two-degree-of-freedom wing actuation—a capability previously difficult to achieve with conventional mechanisms—can be realized through significant mechanical refinements. A single-wing testbed of the proposed mechanism (Fig. 1) was fabricated, and experimental results confirmed its consistency with the theoretical motion model. Furthermore, we show that arbitrary yaw-steering torque can be generated while maintaining sufficient lift force for sustained hovering. These findings represent a foundational step toward realizing biologically inspired, high-agility flapping-wing flight using simple mechanical architectures.

II. Two-Degree-of-Freedom Driving Mechanism

A. 2-DoF Mechanism in Past Works

Schematics of the motion conversion mechanism we proposed previously are shown in Fig. 3 [15, 16]. The FMAV testbed was equipped with a pair of transmissions on the left and right sides. Three plates (A, C, and D) supported the wing root portion (B). The upper rotor, connected to plate (A), directly moved the leading edge of the wing, while the trailing edge was moved by plate (C), which was linked to the lower rotor via plate (D). Two 0.1-g ultrasonic transducers independently drove the rotors, aiming to generate the stroke and twist motion of the wings.

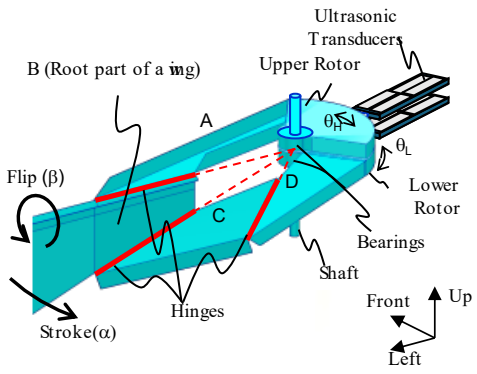

Figure 3. Hinge linkage flapping system [15, 16].

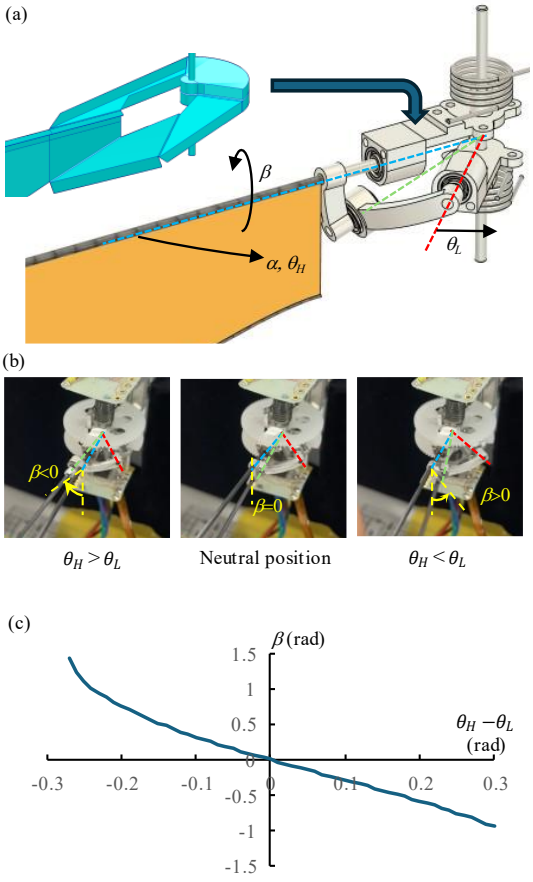

Figure 4. (a) Proposed 2-DoF mechanism (spur gears are omitted), (b) its flipping motion, and (c) relationship between the angle difference of the two arms and the flipping angle.

B. Issues of Past Design

1) Drive Stability

Due to the unstable friction conditions between the rotor and transducer, the transfer efficiency of the force between them varied significantly, especially under high motor torque. Additionally, a resonant mechanism for increasing flapping amplitude, which might cause additional disturbance on the contact situation, could not be adopted in this case [12].

2) Link Play

The target of the previous study was to achieve a 2-gram scale FMAV. For weight reduction, plates with a narrow gap bridged by an elastic film structure were employed as the link mechanism converting two rotors' reciprocation to stroke and flip motions. However, because of this gap, the system suffered from significant play, resulting in uncertainty in the wing motion.

C. Improved Mechanism

1) Applying Resonant mechanism with DC motors

In this work, we aim for an up-scaled version of the 2-DoF FMAV mechanism, targeting approximately 20 grams. This means the mass limitation is significantly relaxed, making commercially available small DC motors a viable choice. Therefore, the ultrasonic motor configuration was replaced with a combination of a DC motor and a torsion spring for

resonant drive, a configuration previously employed in studies that demonstrated 20-g FMAV untethered flight [6].

2) Cross-Coupled 2DoF Mechanism

To ensure the controllability of the 2-DoF flapping, specifically arbitrary stroke and flip motion, a cross-coupled mechanism is proposed. We first clarify the issue of controllability in a non-coupling system from the motion governing equations.

As shown in Fig. 4, the stroke angle α is equivalent to the upper arm rotation, θ_H. For a simple replacement of USM to DCM with torsion springs, as shown in Fig. 4, the relation of the rotation angle difference between the upper and lower arms, $\theta_H - \theta_L$, and the wing flipping angle from vertical attitude, β, is same as the past work shown in Fig. 4(c) [16]. The function exhibits near-linear behavior around the zero point, allowing for a linear approximation as follows:

$$\beta \approx -2.8175(\theta_H - \theta_L). \quad (1)$$

Therefore, a motion conversion equation can be defined:

$$\begin{Bmatrix}\alpha\\ \beta\end{Bmatrix} \approx \begin{bmatrix}1 & 0\\ -b & b\end{bmatrix}\begin{Bmatrix}\theta_H\\ \theta_L\end{Bmatrix} = [D]\begin{Bmatrix}\theta_H\\ \theta_L\end{Bmatrix}, \quad (2)$$

where b=2.8175, and $[D]$ is a motion conversion matrix.

On the other hand, the motion equation can be described as;

$$\begin{bmatrix}J_{\alpha\alpha} & J_{\alpha\beta}\\ J_{\beta\alpha} & J_{\beta\beta}\end{bmatrix}\begin{Bmatrix}\ddot{\alpha}\\ \ddot{\beta}\end{Bmatrix} + \begin{bmatrix}C_{\alpha\alpha} & C_{\alpha\beta}\\ C_{\beta\alpha} & C_{\beta\beta}\end{bmatrix}\begin{Bmatrix}\dot{\alpha}\\ \dot{\beta}\end{Bmatrix} + \begin{bmatrix}K_{\alpha\alpha} & K_{\alpha\beta}\\ K_{\beta\alpha} & K_{\beta\beta}\end{bmatrix}\begin{Bmatrix}\alpha\\ \beta\end{Bmatrix} = \begin{Bmatrix}\tau_\alpha\\ \tau_\beta\end{Bmatrix}, \quad (3)$$

where J_{ij} (hereafter, *i, j* represents α or β) is the inertia, C_{ij} is the dumping, and K_{ij} is the stiffness matrices, respectively. τ_α, τ_β means the torques acting on corresponding rotation axes. On the upper line is motion governing equation of wing stroke angle and lower is that of flip angle.

The wing actuation torques, τ_α, τ_β, are kinematically delivered as follows:

$$\begin{Bmatrix}\tau_\alpha\\ \tau_\beta\end{Bmatrix} = [[D]^{-1}]^T\begin{Bmatrix}\tau_H\\ \tau_L\end{Bmatrix} = \begin{bmatrix}1 & 1\\ 0 & 1/b\end{bmatrix}\begin{Bmatrix}\tau_H\\ \tau_L\end{Bmatrix}, \quad (4)$$

where τ_H and τ_L are the torques acting on the upper and lower arms, respectively. Note that each of the torque is given by the motor current I_H or I_L,

$$\tau_{H/L} = \eta K_T N_{gear} I_{H/L}, \quad (5)$$

where η is torque transmit efficiency of the spur gear, K_T is the torque constant of the motor, and N_{gear} is the gear ratio, respectively.

Therefore, the motion equation is converted to;

$$[D]^T\begin{bmatrix}J_{\alpha\alpha} & J_{\alpha\beta}\\ J_{\beta\alpha} & J_{\beta\beta}\end{bmatrix}[D]\begin{Bmatrix}\ddot{\theta_H}\\ \ddot{\theta_L}\end{Bmatrix} + [D]^T\begin{bmatrix}C_{\alpha\alpha} & C_{\alpha\beta}\\ C_{\beta\alpha} & C_{\beta\beta}\end{bmatrix}[D]\begin{Bmatrix}\dot{\theta_H}\\ \dot{\theta_L}\end{Bmatrix} + [D]^T\begin{bmatrix}K_{\alpha\alpha} & K_{\alpha\beta}\\ K_{\beta\alpha} & K_{\beta\beta}\end{bmatrix}[D]\begin{Bmatrix}\theta_H\\ \theta_L\end{Bmatrix} = \begin{Bmatrix}\tau_H\\ \tau_L\end{Bmatrix}. \quad (6)$$

By comparison to the real configuration, the stiffness term should be;

$$[D]^T\begin{bmatrix}K_{\alpha\alpha} & K_{\alpha\beta}\\ K_{\beta\alpha} & K_{\beta\beta}\end{bmatrix}[D] = \begin{bmatrix}K_H & 0\\ 0 & K_L\end{bmatrix}, \quad (7)$$

where K_H and K_L are the spring constants of the torsion springs equipped on the arms shown in Fig. 4. Therefore,

$$\begin{bmatrix}K_{\alpha\alpha} & K_{\alpha\beta}\\ K_{\beta\alpha} & K_{\beta\beta}\end{bmatrix} = [[D]^{-1}]^T\begin{bmatrix}K_H & 0\\ 0 & K_L\end{bmatrix}[D]^{-1} = \begin{bmatrix}K_H + K_L & K_L/b\\ K_L/b & K_L/b^2\end{bmatrix}. \quad (8)$$

Here, the restoring force term of governing equation of flipping motion (lower line of eq. 3) becomes:

$$\frac{K_L}{b}\alpha + \frac{K_L}{b^2}\beta = \frac{K_L}{b}\left(\theta_H + \frac{1}{b}\left(-b(\theta_H - \theta_L)\right)\right) = \frac{K_L}{b}\theta_L. \quad (9)$$

As shown in Eq. 9, the restoring-force term lacks a component associated with the flipping-angle, that is, $(\theta_H - \theta_L)$. As a result, the equilibrium position of the flip motion becomes undefined, and the angle of attack develops path dependency, leading to stroke-by-stroke instability in aerodynamic forces such as lift and drag.

To address that, in this study, the cross-coupling spring with the spring constant of K_I was added between the leading edge of the wing and the upper arm as shown in Fig. 5. The stiffness matrix of eq. 7 becomes $\begin{bmatrix}K_H + K_C & -K_C\\ -K_C & K_L + K_C\end{bmatrix}$, where $K_C = bK_I$. Equation 8 changes to;

$$\begin{bmatrix}K_{\alpha\alpha} & K_{\alpha\beta}\\ K_{\beta\alpha} & K_{\beta\beta}\end{bmatrix} = [[D]^{-1}]^T\begin{bmatrix}K_H + K_C & -K_C\\ -K_C & K_L + K_C\end{bmatrix}[D]^{-1} = \begin{bmatrix}K_H + K_L & K_L/b\\ K_L/b & (K_L + K_C)/b^2\end{bmatrix}. \quad (10)$$

Therefore, on the flipping motion governing equation, the stiffness term becomes $\frac{1}{b}(K_L\theta_L - K_C(\theta_H - \theta_L))$.

With this configuration, the governing equation includes a restoring-force term for the flipping motion, allowing the angle β to participate in a vibration orbit centered at zero. Consequently, the path dependency of the flip angle is expected to disappear.

3) Precise Link Mechanism

In addition, we employed ball bearings instead of hinges to achieve play-less link mechanism. In the practical mechanism, to reduce rotation axis tilt, a pair of bearing is employed as an alternative to the flexible hinge.

III. Single-Wing Testbed

A. Overview

The configuration of the testbed is shown in Fig. 5. It is mounted on a force/torque sensor (Nano17 TI, ATI) for flapping force measurement. The rotation angles of the arms are magnetically measured by magnetic angle sensors (MA735, MPS). A Matlab/ Simulink system sends PWM and direction signals independently to two motor drivers (MP6543HB, MPS). The motor current is measured via 0.3 Ω shut registers

inserted between the motor driver and the motor. We employed two brushless motors, Maxon ECX Speed 6. The specs are shown in Table I.

B. Testbed

As shown in Fig. 5(c), the 2DoF mechanism has two motors fixed on the body of the testbed. The motors rotation speeds are reduced by a 1:10 spur gear ratio. Aluminum arms are fixed on the spur gears. The upper arm supports the reading edge of the wing with free rotation around its axis. The leading edge of the wing forms the one side of the wing flipping mechanism. The lower arm supports the end of that side. We employed the dimension of the link mechanism proposed in our past studies [15, 16]. Thus, the relationship between the flip angle and the difference angle of the arms is as indicated in Fig. 4(c). Both arms incorporate sets of ball bearings to hold the corresponding axes with minimal friction. The hinge plates employed in the past work are replaced with the aluminum beams indicated in Fig. 4(a). The specifications of the testbed parts are shown in Table. II. Note that $\begin{bmatrix} J_{\alpha\alpha} & J_{\alpha\beta} \\ J_{\beta\alpha} & J_{\beta\beta} \end{bmatrix} = [[D]^{-1}]^T \begin{bmatrix} J_H & 0 \\ 0 & J_L \end{bmatrix} [D]^{-1}$ from eq. 6.

C. Wing

A 0.8mm diameter Carbon Reinforced Fiber Plastic (CFRP) shaft is employed as the leading edge of the wing. A 0.3mm CFRP shaft is used as the outer frame of the wing. The frames are covered with a 0.34 oz/yd^2 Dyneema Composite Fabric (DCF). The mass and inertia of those parts are also shown in Table. II.

TABLE I. MOTOR SPECIFICATIONS

Item	Value	Unit
Nominal voltage	12	V
No load speed	63400	rpm
No load current	29.8	mA
Torque constant	1.75	mNm/A
Stall torque	1.7	mNm
Rotor inertia	0.703	g·mm^2
Terminal resistance	12.4	Ω
Thermal time constant winding	1.4	s
Thermal time constant motor	70.4	s
Weight	3.0	g

IV. EXPERIMENT

A. System Parameter Validations

To validate the mechanism, the transfer matrix between the wing motions and motor motions was measured.

The motion conversion matrix described in eq. 2 is automatically defined by the dimensions of the link parts. Theoretically, the torque transferring matrix shown in eq. 4 is also automatically given as the inverse transpose matrix of $[D]$. However, axis shifts in the linkage may cause dimensional changes. To validate it, the matrix components are estimated by measuring the flipping torque with a fixed leading edge, as shown in Fig. 6(a), and the current of the motors. In addition,

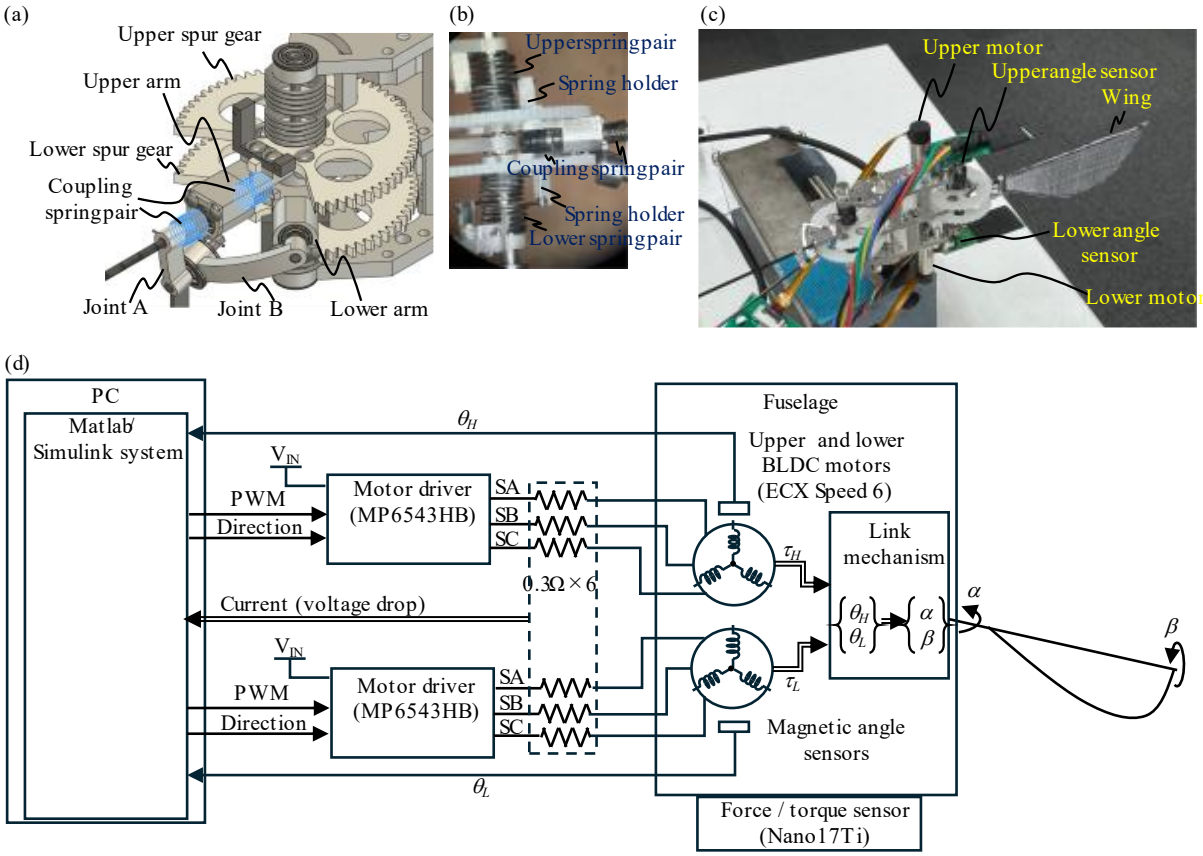

Figure 5. (a) Cross-coupling torsion springs inserted into the linkage, (b) a side view, (c) overview and (d) configuration of the single-wing testbed.

to confirm the restoring force on the leading edge, the stiffness matrix was also evaluated. Finally, to validate the inertia matrix, the free vibration frequencies of the upper and lower arms were measured under conditions where one arm vibrated freely while the other was fixed.

B. 2-DoF Driving Pattern

As a demonstration of the controllability of steering torque generation, a driving method with a combination of two sine-wave voltage with a delay and offset is employed.

In past studies it was proposed that a slight delay of the lower-side arm's stroke motion relative to the upper side causes the flipping motion of the wing as shown in Fig. 7(a) [15]. Additionally, an offset in the lower arm's driving voltage results in an offset of the flipping amplitude center, as shown in Fig. 7(b). Thus, the two-dimensional parameter study was conducted using:

$$\begin{cases} V_H = V_{H0}\sin(2\pi f t) \\ V_L = V_{L0}\sin\left(2\pi f(t-\delta_t)\right) + O_L \end{cases} \quad (11)$$

where V_H and V_L are driving voltage of the upper and lower motors with their amplitude of V_{H0} and V_{L0}, f is the flapping frequency, δ_t is the delay of the lower arm's actuation relative to the upper one, and O_L is the offset voltage, respectively.

We assumed that the delay of the lower arm varies the lift force and that the offset causes the horizontal force. The difference in lift force between the left and right wings generates roll steering torque, and the difference in horizontal force generates yaw steering torque. Therefore, the arbitrary generation of lift force and yaw torques will serve as evidence of steering torque controllability.

TABLE II. INERTIA LIST (3D CAD CALCULATIONS)

Components	Item	Inertia (g·mm²)		
		$J_{\alpha\alpha}$	$J_{\alpha\beta}$	$J_{\beta\beta}$
Wing-mounted	Wing membrane[a]	28.93	4.905	1.232
	Frame shaft	29.31	7.481	2.630
	Leading shaft	93.00	0.000	0.004
	Tip connector	21.71	0.093	0.002
	Spacer	0.324	0.324	0.324
	Shaft cover	0.156	0.156	0.156
	Joint A	9.670	1.538	0.436
Intermediate-linkage-mounted	Joint B	14.86	2.708	1.827
	Inner bearing	5.224	1.754	0.642
	Outer bearing	6.912	2.328	0.850
	Connection shaft	7.607	2.532	0.935
Components	**Item**	**Inertia (g·mm²)**		
		J_{HH}	J_{HL}	J_{LL}
Upper-arm-mounted	Upper arm[a]	6.928	0.000	0.000
	Upper Spring[a]	2.630	0.000	0.000
	Shaft	0.006	0.000	0.000
	Spur gear[a]	14.36	0.000	0.000
	Inner bearing	2.268	0.000	0.000
	Outer bearing	4.418	0.000	0.000
	Coupling spring[a]	7.344	0.000	0.000
	Motor rotor[b]	70.3	0.000	0.000
Lower-arm-mounted	Lower arm[a]	0.000	0.000	6.928
	Lower Spring[a]	0.000	0.000	2.630
	Shaft	0.000	0.000	0.006
	Spur gear[a]	0.000	0.000	14.355
	Inner bearing	0.000	0.000	2.268
	Outer bearing	0.000	0.000	4.418
	Coupling spring[a]	0.000	0.000	7.344
	Motor rotor[b]	0.000	0.000	70.3

a. Contains screws, connectors or glue.

b. Equivalent value through gear ratio of 10.

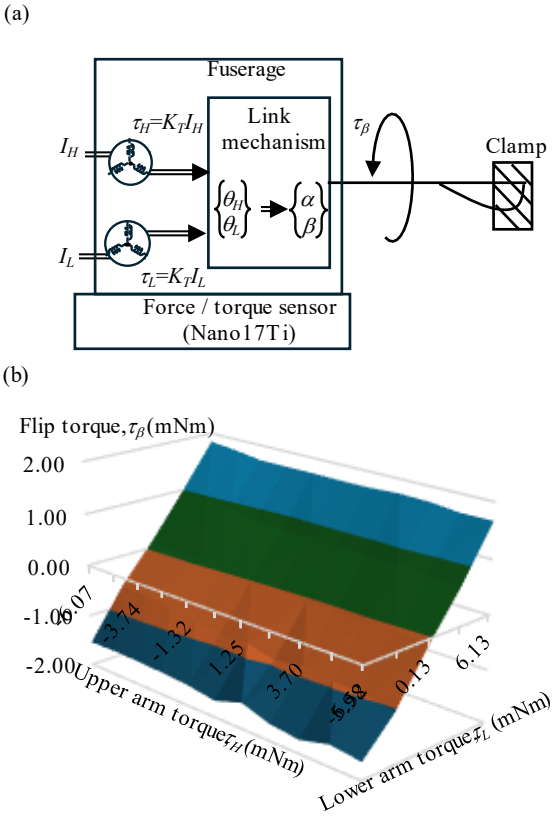

Figure 6. (a) Torque conversion measurement and (b) relationship between the two arms torque and the flipping torque.

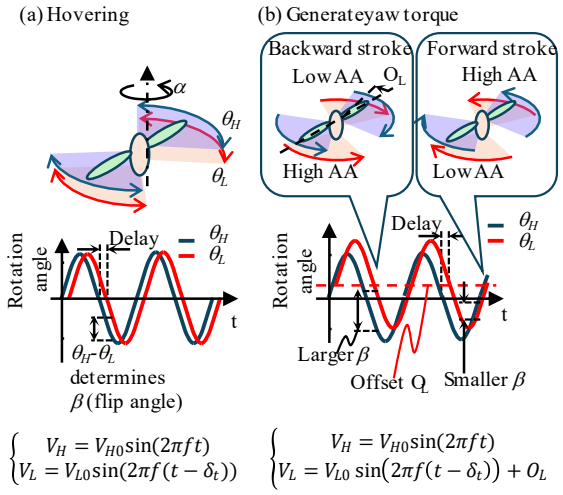

Figure 7. A simple method for yaw torque steering and the assumed driving voltages of the motors.

TABLE III. SPRING CONSTANTS

Item	Spring constant (mNm/rad)	
	A. Validation	*B. Actual test*
Upper spring	3.74 × 2	16.0× 2
Lower spring	3.74 × 2	16.0× 2
Coupling spring	0.811 × 2	0.811 × 2

Note that springs are used as a right-hand/left-hand spring pair to linearize the torque–angle relationship.

V. RESULT

A. System Parameter Validations

1) Torque Conversion Matrix

Figure 6(b) shows the flipping torque caused by the current of the two motors. The motor torque constant is 1.75 [mNm/A] and the gear reduction ratio is 10. Assuming a gear efficiency of 0.95, the relationship of torque is;

$$\tau_\beta = 0.95 \times 5.775 \times 10^{-3} I_L = 0.314 \tau_L. \quad (12)$$

Theoretically, the value would be 1/2.8517 = 0.3507. Considering the accuracy of the torque sensor, the value of 0.314 shows good accordance.

2) Stiffness Matrix Validation\

By static measurement of the flipping angle and motor torques, under conditions where $\ddot{\alpha} = \dot{\alpha} = 0$ and $\ddot{\beta} = \dot{\beta} = 0$, the following relationship shown in Fig. 8 was delivered through eq. 6 as:

$$\begin{Bmatrix}\theta_H\\ \theta_L\end{Bmatrix} = \begin{bmatrix}1.345 & 0.878\\ 1.006 & 1.213\end{bmatrix}\begin{Bmatrix}I_H\\ I_L\end{Bmatrix} = \begin{bmatrix}80.9 & 52.8\\ 60.5 & 72.9\end{bmatrix}\begin{Bmatrix}\tau_H\\ \tau_L\end{Bmatrix}. \quad (13)$$

(Note that η=0.95, K_T=1.75 [mNm/A], N_{gear}=10.) Therefore,

$$\begin{bmatrix}K_H+K_C & -K_C\\ -K_C & K_L+K_C\end{bmatrix} = \begin{bmatrix}80.9 & 52.8\\ 60.5 & 72.9\end{bmatrix}^{-1}$$

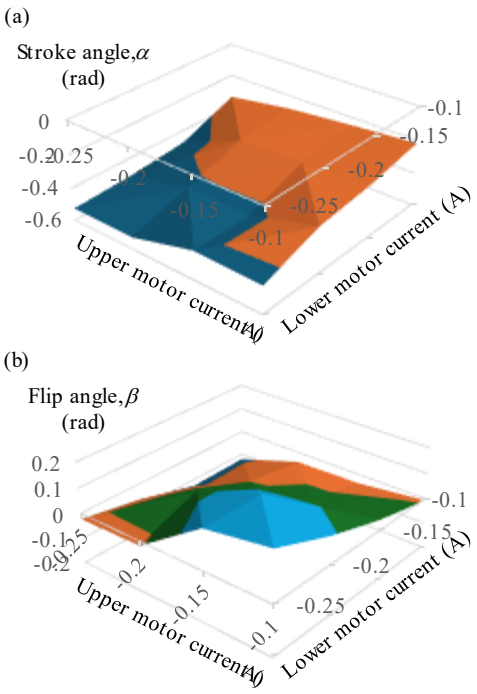

Figure 8. Identification of stiffness matrix through linear fitting.

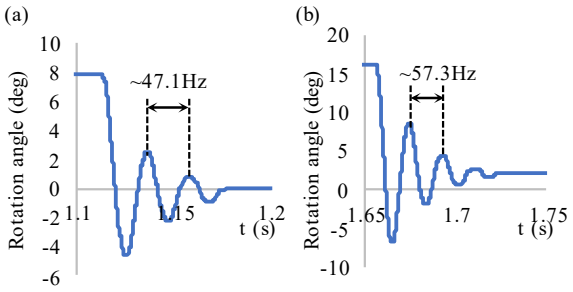

Figure 9. Free vibration characteristics of the upper and lower arms.

$$= \begin{bmatrix}27.0 \times 10^{-3} & -19.5 \times 10^{-3}\\ -22.4 \times 10^{-3} & 29.9 \times 10^{-3}\end{bmatrix}. \quad (14)$$

As shown in Table. III, the real value, $K_H = K_L = 7.48 \times 10^{-3}$, $K_C = b^2 K_I = 25.37$, shows good accordance.

3) Free-Vibration Frequencies

As shown in Fig. 9, the free vibration frequency of the upper arm with the lower fixed is 47.1 Hz, and conversely, that of the lower arm with the upper fixed is 57.3 Hz.

The natural resonant frequencies of these situations are estimated from eq. 6 as $\frac{1}{2\pi}\sqrt{\frac{K_H+K_C}{J_{\alpha\alpha}+b^2J_{\beta\beta}-bJ_{\alpha\beta}-bJ_{\beta\alpha}}}$ and $\frac{1}{2\pi}\sqrt{\frac{K_L+K_C}{b^2J_{\beta\beta}}}$, respectively. From the values of Tables II and III, the theoretical values without dumping are 49.8 and 60.3 Hz, respectively. The experimental results do not conflict with these theoretical predictions.

B. 2-DoF Flapping Force Generation

1) Resonant Frequency Measurement

In above experiment, we employed relatively soft springs, i.e., $K_H = K_L = 7.48 \times 10^{-3}$, aiming to obtain sufficiently large rotation angles of the arms under non-resonant situation. However, in actual flapping, the maximum stroke amplitude is limited to π/2. To generate higher aerodynamical forces within this constraint, the resonant frequency must be increased. Therefore, stiffer springs listed in Table. III ($K_H = K_L = 32.0 \times 10^{-3}$) are used. Figure 10 illustrates the dependence of the vibration amplitude of the two arms when the variables in Eq. 11 are set to the following values: V_{H0} = 12.0 V, V_{L0} = 10.8 V, δ_t = 0.0, and O_L = 0.0.

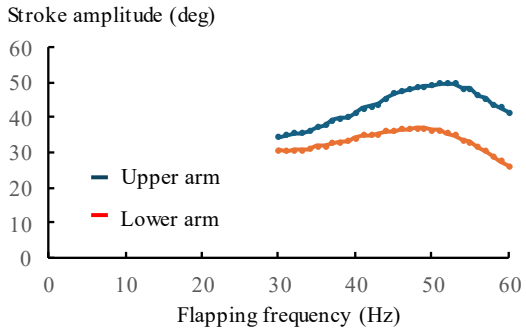

Figure 10. Frequency dependency of flapping amplitude. (V_{H0}=12.0 V, V_{L0} = 10.8 V, delay and offset set to 0.)

2) Lift force and Yaw Torque generated by 2-DoF Flapping

Figure 11 shows the results of the parameter study on phase-delay (δ_t) and voltage offset (O_L) of the lower arm relative to the upper arm.

First, when the phase delay δ_t is set to 15% of the flapping cycle, a lift force of 10 gf is obtained, which is comparable to values reported in previous studies [6]. Next, a strong correlation is observed between the yaw torque and the offset voltage applied to the lower arm, indicating controllability of the yaw torque generated by flapping. Furthermore, although an offset in the yaw torque is present, its range of 1.5 mNm exceeds the value reported in Zhan's study [6]. Note that the yaw-torque magnitude doubles to approximately 3.0 mNm when using a paired-wing configuration. On the other hand, the lift force shows little correlation with the offset value. This indicates that, with a phase delay δ_t of 15% of the flapping period, the yaw torque can be actively controlled while the lift force remains nearly constant.

VI. Discussions and Limitations

The controllability of yaw torque using the 2-DoF flapping mechanism with cross-coupling is successfully demonstrated. The lift force of 10 gf obtained with a single wing suggests the feasibility of a 20-g-class FMAV. As indicated in Eq. 4, however, the wing-flapping torque τ_α, is the sum of the motor torques of the upper and lower arms. Therefore, the lift force generated by each wing can, in principle, be increased up to 20 gf. In the experiment described above, some inefficiency in the springs may have arisen from inter-coil friction, and this requires further investigation.

In addition, stiffer torsion springs than those employed in previous studies are required to achieve the same resonant flapping frequency. This is because the resonant frequency is significantly affected by the off-diagonal inertia term $bJ_{\alpha\beta}$. Furthermore, the motor rotor inertia is amplified by the square of the gear ratio, which is 100 in our case. Notably, the total rotor inertia of 70 g mm^2, is comparable to that of the wing itself, approximately 150 g mm^2. Consequently, the spring constant of the upper arm must be increased. In our prototype, the total mass of the four torsion springs was 1.7 g. The feasibility of untethered flight for a 2×2-DoF FMAV thus depends strongly on achieving an appropriate mass distribution among these mechanical components.

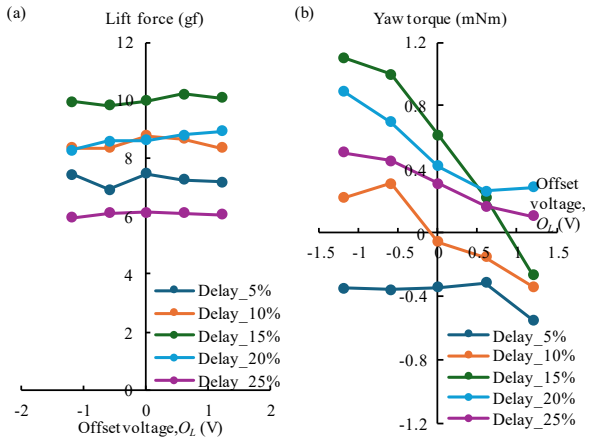

Figure 11. (a) Lift-force and (b) yaw-torque dependence on the offset voltage O_L. A phase-delay δt of 15% (as indicated in Eq. 11) yields the peak lift force and the largest range of yaw torque. Note that the lift force remains nearly constant while the yaw torque varies.

VII. Conclusions and Future Works

A cross-coupling method that enhances controllability was proposed by introducing a restoring force between the two wing-driving arms. This approach enables a controllable flipping motion of the wing. Experimental results confirmed that yaw-steering torque can be generated by offsetting the actuation voltage of the lower arm, while the lift force remains nearly constant. These findings demonstrate that the proposed mechanism allows independent manipulation of yaw torque without compromising lift generation.

Future work will focus on the realization of the untethered flight of the 2x2-DoF FMAV. The inefficiencies in the testbed of this study should be revealed and removed to achieve higher lift force.

Although the present 2×2-DoF system does not match the highly complex, multi-degree-of-freedom wing kinematics observed in insects and birds—where more than ten functional degrees of freedom are involved—it nonetheless represents a meaningful step toward expanding wing-actuation freedom in FMAVs.

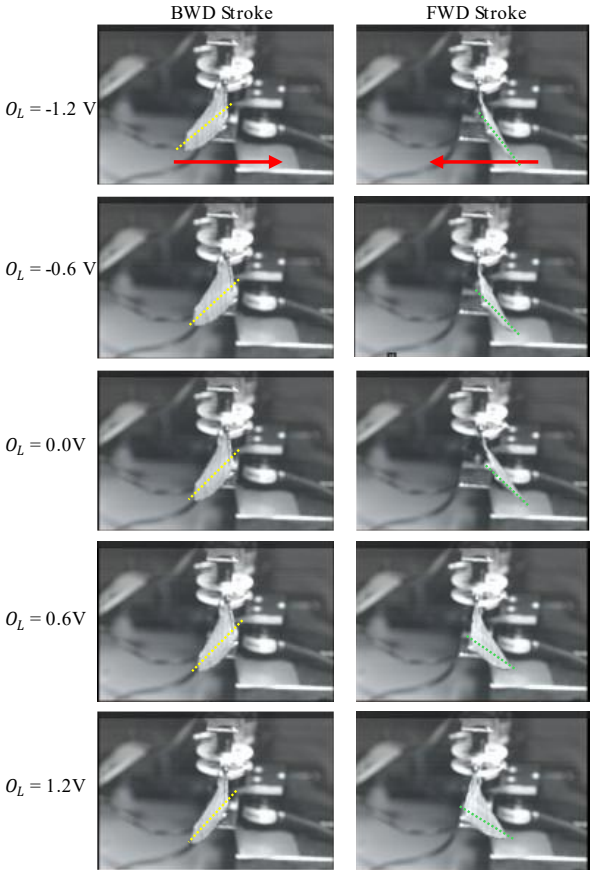

Figure 12. High-speed-camera image of 2-DoF flapping motion on the center of the stroke. A phase-delay δt is 15% of the flapping cycle. The difference of the attack angles between forward- and backward-strokes is clearly observed.

ACKNOWLEDGMENT

This work was conducted as part of a collaborative research project under Japan Aerospace Exploration Agency (JAXA)'s Research Funding Program (RFP9), and we would like to express our sincere gratitude to JAXA for its support and contributions. Follow-up studies were also carried out with continued support from JAXA.

REFERENCES

[1] C. P. Ellington, "The aerodynamics of hovering insect flight. VI. Lift and power requirements," *Philos. Trans. R. Soc. Lond.*, vol. B305, pp. 145-181, Feb. 1984.

[2] A. Azuma, *The Biokinetics of Flying and Swimming*. Tokyo: Springer-Verlag, 1992.

[3] A. K. Brodsky, *The Evolution of Insect Flight*. Oxford: Oxford University Press, 1994.

[4] M. Keennon et al., "Development of the Nano hummingbird: A tailless flapping wing micro air vehicle," *Proc. 50th AIAA Aerosp. Sci. Meeting Including New Horizons Forum Aerosp. Expo.*, 2012.

[5] H. V. Phan et al., "Design and stable flight of a 21-g insect-like tailless flapping wing micro air vehicle with angular rates feedback control," *Bioinspir. Biomim.*, vol. 12, no. 3, 036006, 2017.

[6] Z. Tu, F. Fei and X. Deng, "Untethered flight of an at-scale dual-motor hummingbird robot with bio-inspired decoupled wings" in *IEEE Robot. Autom. Lett.*, vol. 5, no. 3, pp. 4194-4201, Jul. 2020.

[7] C. Wang, W. Zhang, Y. Zou, R. Meng, J. Zhao and M. Wei, "A sub-100 mg electromagnetically driven insect-inspired flapping-wing micro robot capable of liftoff and control torques modulation," *J. Bionic Eng.*, vol. 17, no. 6, pp. 1085-1095, 2020.

[8] R. S. Fearing, K. H. Chiang, M. H. Dickinson, D. L. Pick, M. Sitti and J. Yan, "Wing transmission for a micromechanical flying insect" in *Proc. IEEE Intl. Conf. on Robotics and Automation*, San Francisco, 2000, pp. 1509-1515.

[9] R. J. Wood, "Liftoff of a 60mg flapping-wing MAV" in *Proc. IEEE Int. Conf. on Intelligent Robots and Systems*, San Diego, 2007, pp. 1889-1894.

[10] N. T. Jafferis, E. F. Helbling, M. Karpelson, and R. J. Wood, "Untethered flight of an insect-sized fapping-wing micro-scale aerial vehicle," *Nature*, vol. 570, no. 7762, pp. 491-495, 2019.

[11] T. Ozaki, N. Ohta, T. Jimbo and K. Hamaguchi, "A wireless radiofrequency-powered insect-scale flapping-wing aerial vehicle," *Nat. Electron.*, vol. 4, no. 11, pp. 845-852, 2021.

[12] D. Campolo, M. Azhar, G. -K. Lau and M. Sitti, "Can DC motors directly drive flapping wings at high frequency and large wing strokes?" *IEEE ASME Trans. Mechatron.*, vol. 19, no. 1, pp. 109-120, Feb. 2014.

[13] D. Campolo, "Motor selection via impedance-matching for driving nonlinearly damped, resonant loads," *Mechatronics*, vol. 20, no. 5, pp. 566-573, 2010.

[14] M. Hamamoto, T. Kotani, I. Nakano, Y. Ohta, K. Hara, Y. Murakami and T. Hisada, "Investigation on force transmission of direct-drive thorax unit with four ultrasonic motors for a flapping microaerial vehicle," *Adv. Robot.*, vol. 28, no. 3, pp. 133-144, 2014.

[15] M. Hamamoto, "Toward Dexterous Flapping Flight: Effective Large Yaw Torque Generation by 2×2-Degrees-of-Freedom Flapping Wings," in *Proc. The 2022 IEEE/RSJ International Conference on Intelligent Robots and Systems,* Kyoto, 2022, pp. 2650-2657.

[16] M. Hamamoto, Y. Ohta, K. Hara and T. Hisada, "A fundamental study of wing actuation for a 6-in-wingspan flapping microaerial vehicle," *IEEE Trans. Robot.*, vol. 26, no. 2, pp. 244-255, 2010.